scientific reports

Check for updates

OPEN

Untethered soft magnetic pump for microfluidics-based Marangoni surfer

Yu-Hsiang Lin[1]✉, Franco N. Piñan Basualdo[1], Venkatasubramanian Kalpathy Venkiteswaran[1] & Sarthak Misra[1,2]✉

Microfluidics has enabled the miniaturization of fluidic systems for various biomedical and industrial applications, including small-scale robotic propulsion. One mechanism for generating propulsive force through microfluidics is by exploiting the solutal Marangoni effect via releasing surfactant on the air-water interface. Surfactants locally reduce the surface tension, which leads to a surface stress that can propel the floating robot, called Marangoni surfer. However, so far the release of the surfactant is not controllable. In this study, we combine microfluidics-based Marangoni propulsion with a novel untethered magnetic pumping mechanism to enhance its controllability. The proposed magnetic micropump capitalizes on the interaction force between two soft magnets, which can generate a pumping force of 4.64 mN to actuate a membrane, and achieve a deformation of 450 µm. Net flow is achieved using a nozzle/diffuser flow rectifier whose efficacy as a function of the channel geometry is numerically studied. We investigate the flow rate of the pump with regard to the actuation frequency. Finally, we demonstrate its ability to control the motion of the Marangoni surfer.

Keywords Magnetic micropump, Marangoni propulsion, Soft magnet

Microfluidics provides a powerful platform for high-throughput pharmaceutical and pathological analysis[1–3]. One of the strengths of microfluidics is the capability to handle liquids precisely at the micro-/nano-liter scale, which is particularly useful for lab-on-a-chip devices[4]. After decades of developments, various flow control elements in microfluidic systems have been created, such as micropumps and microvalves[5–8], which help to precisely route and control the flow[9,10]. These functionalities have enabled the development of soft robotic systems whose bodies deform as a result of pressure in embedded microfluidic circuits.[11,12]. These robots can achieve different functions, such as grasping[13], terrestrial locomotion[14], and underwater swimming[15]. Furthermore, small-scale robots can controllably release the liquid through the channels to generate propulsion[16].

Contrary to conventional hydraulic and pneumatic systems, microfluidics operates in the low Reynolds number regime, where the viscous forces dominate. This renders the conventional fluid jet mechanism impractical when it comes to microfluidics-based propulsion. In the quest to develop efficient propulsion mechanisms for miniaturized robots, researchers have attempted to take inspiration from nature. The surfactant-induced Marangoni effect, also known as the solutal Marangoni effect, has been observed to be exploited in the escape maneuver of certain species of semi-aquatic insects, e.g., *Microvelia* (small water striders) and *Stenus* (rove beetles). The surfactant released by these insects creates a surface tension gradient which results in a force propelling the insects to achieve a peak speed of 17 cm s^{-1}, or twice the walking speed, to escape from their predators[17]. The physics of driving miniature surfers with the solutal Marangoni effect has been studied extensively[18–20], showing efficient propulsion of small-scale objects using the solutal Marangoni effect and potential applications in monitoring[16] and exploring[21] aquatic environments. Despite abundant studies on the mechanism of the Marangoni surfer, the controllability of the propulsion remains a challenging topic.

In previous work, Kwak et al. have attempted to employ an untethered magnetic pump in centimeter-scale Marangoni surfer[16]. Yet, the flow in this design is triggered by the placement of a permanent magnet atop a pump chamber, which cannot be controlled on demand. To improve the controllability, a microfluidic pump with active elements is necessary. In the past decades, microfluidic pumps driven by various mechanisms have been developed, e.g., piezoelectric elements and pneumatic channel layer.[5,22]. However, conventional micropumps are

[1]Surgical Robotics Laboratory, Department of Biomechanical Engineering, University of Twente, 7522 NB Enschede, The Netherlands. [2]Surgical Robotics Laboratory, Department of Biomaterials and Biomedical Technology, University of Groningen and Univesity Medical Center Groningen, 9713 AV Groningen, The Netherlands. ✉email: y.lin-1@utwente.nl; s.misra@utwente.nl

often tethered to electrical power sources or pressured air supplies. This restricts the potential of utilizing them for the actuation of the miniature robots demanding freedom in motion. Diller et al. have developed a remotely controllable micro-scale magnetic pump that could be selectively actuated, which requires a magnetic field pulse signal of up to 240 kA m^{-1} to overcome the magnetic coercivity[23].

In this work, we propose an untethered magnetic pump that can be controlled with an external magnetic field. The proposed untethered magnetic pump proposed in this study leverages the magnetic interaction force between two soft magnetic components. When placed in a homogeneous magnetic field parallel to the arrangement of the soft magnets, the latter gets magnetized, which generates an attractive force between the two soft magnets. This magnetic force deforms a polydimethylsiloxane (PDMS) membrane on the pump chamber and displaces a surfactant solution through connecting channels. A nozzle/diffuser channel allowing an asymmetric flow rate in different flow directions is designed to rectify the flow.

Herein, we first use a magnetic dipole model and finite element analysis to describe the magnetic interaction force between two soft magnets placed in a homogeneous magnetic field. We relate this force to the resulting membrane deformation to estimate the displaced volume during the pumping phase. Next, the diodity of the nozzle/diffuser flow rectifier as a function of its geometry is numerically investigated to ensure a net flow can be generated from the pump chamber to the outlet. A soft magnetic micropump is designed based on the developed models, and its performance is experimentally characterized. The flow rate as a function of actuation frequency and the amplitude of the external magnetic field is measured. Finally, a controllable stop-and-move motion of a microfluidics-based Marangoni surfer utilizing the soft magnetic pump is demonstrated.

Results and discussion

Operation principle of the microfluidics-based Marangoni surfer

The operation of the proposed surfer is based on the solutal Marangoni effect, i.e., the emergence of a flow along a fluid interface in the presence of a surface tension gradient[24]. The flow emerges from the unbalanced surface stress as a result of applying surfactant at the channel outlet (Fig. 1a). At the initial equilibrium state, the surfer is stationary. The net force acting on the surfer is zero because the surface tension pulling in all normal directions around the contour of the surfer is balanced. The direct Marangoni force at the equilibrium state ($\mathbf{F}_{\mathrm{Ma,eq}}$) can be expressed as

$$\mathbf{F}_{\mathrm{Ma,eq}} = \int_{\mathrm{c}} \gamma(\mathrm{c})\sin(\theta(\mathrm{c}))\mathbf{e}_{\mathrm{n}}\,\mathrm{dc} = 0, \tag{1}$$

where c is the contour of the surfer, γ is the surface tension at the contact line, θ is the interface angle as a function of the position along the surfer contour, and $\mathbf{e}_{\mathrm{n}}$ is the unit vector on the x–y plane and normal to the contact wall (Fig. 1a). As shown in the inset in Fig. 1a, the resulting force from the surface tension is pointing in the direction of the unit vector ($\mathbf{e}_{\mathrm{s}}$), which indicates the direction of the surface tangent vector of the liquid-air interface.

In the event of surfactant release, the surface tension is locally reduced, causing the surfer to exit the equilibrium state due to the unbalanced direct Marangoni force. The locally reduced surface tension (γ_{s}) is a function of the flow rate (Q_{out}) at the outlet and the concentration (c_{out}) of the released surfactant. Surface tension at other unaffected positions, i.e., locations that are not in contact with the surfactant release point, remains unaltered ($\gamma \approx \gamma_{\mathrm{w}}$). Hence, after the surfactant is released, the movement of the surfer is generated, and the expression of the direction Marangoni force should be rewritten as,

$$\mathbf{F}_{\mathrm{Ma,noneq}} = \int_{C_{\mathrm{w}}} \gamma_{\mathrm{w}}\sin\theta_{\mathrm{w}}\mathbf{e}_{\mathrm{n}}\mathrm{dc} + \int_{C_{\mathrm{s}}} \gamma_{\mathrm{s}}(Q_{\mathrm{out}}, c_{\mathrm{out}})\sin\theta_{\mathrm{s}}\mathbf{e}_{\mathrm{n}}\mathrm{dc} \neq 0, \tag{2}$$

where $\mathbf{F}_{\mathrm{Ma.noneq}}$ denotes the direct Marangoni force at the nonequilibrium state after the release of the surfactant, C_{s} denotes the surfer contour segment affected by the surfactant near the channel outlet, θ_{w} is the contact angle of the water and θ_{s} is the contact angle of the surfactant-affected area. This results in a non-zero driving force in the direction opposite to the surfactant release point, which is indicated in Fig. 1b as the moving direction. For achieving controlled release of the surfactant, the fluid manipulation is enabled via the onboard microfluidic channels and micropump.

The proposed Marangoni surfer comprises the following components: a reservoir as the channel inlet, nozzle/diffuser flow rectifiers at both inlet and outlet sides, an untethered soft magnetic pump, and the channel outlet where the surfactant is released to the environment (Fig. 1c). The two main comments contributing to the fluid manipulation are the soft magnetic pump and the nozzle/diffuser flow rectifier. The structure of the untethered soft magnetic pump involves a chamber, a thin elastic membrane layer atop, and a pair of soft magnetic rods on the top and at the bottom of the pump chamber. The rod attached to the elastic membrane moves with the oscillation of the membrane, hence named the oscillatory soft magnetic rod (rod 1 in Fig. 1c), while the other does not move, hence named the stationary rod (rod 2 in Fig. 1c). To direct the flow, a nozzle/diffuser flow rectifier with asymmetric flow resistance in the nozzle and diffuser directions is designed, allowing us to rectify the flow direction without introducing movable components in the microfluidic channel.

The novelty of the proposed soft magnetic pump lies in the untethered actuation modality. Its working principle relies on the local magnetic interaction force of two soft magnetic rods, which emerges when an external magnetic field is applied. Under the influence of a homogeneous magnetic field ($\mathbf{B}_{\mathrm{ext}}$), the soft magnetic rods are magnetized in the same direction and exhibit the magnetic moment of $\mathbf{m}_1$ and $\mathbf{m}_2$, respectively (Fig. 1d1). The attractive magnetic force exerted on the oscillatory soft magnetic rod (rod 1) can be expressed as,

$$\mathbf{F}_{12} = \nabla(\mathbf{m}_1 \cdot \mathbf{B}_2), \tag{3}$$

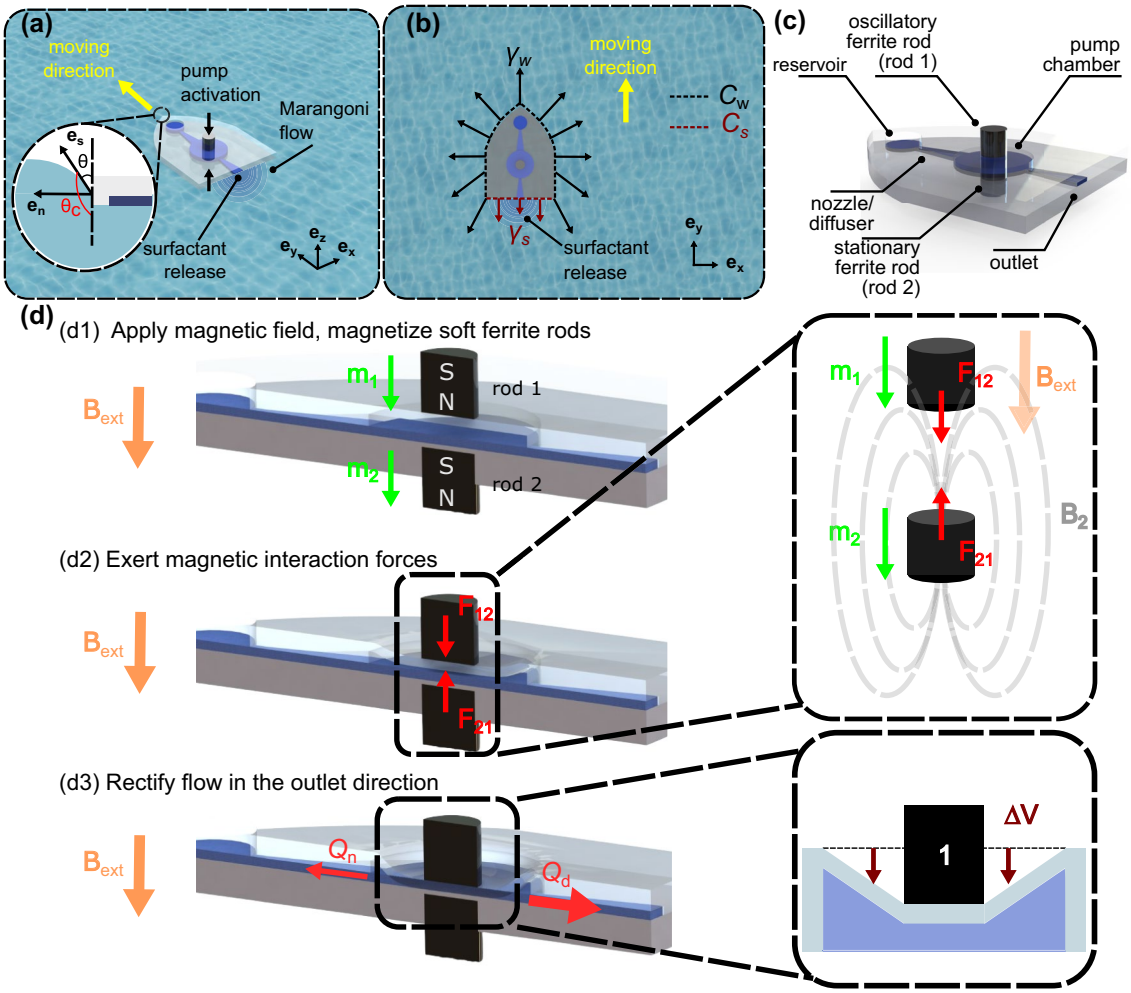

Fig. 1. Design and operation principle of the microfluidics-based Marangoni surfer. (**a**) The motion of the microfluidics-based Marangoni surfer is generated by the surface tension gradient induced by the surfactant release. A remotely actuated soft magnetic pump enables the controlled release of the surfactant. In the inset, $\mathbf{e}_n$ is the unit vector on the x–y plane and normal to the contact wall, γ is the surface tension at the contact line, $\mathbf{e}_s$ indicates the direction of the surface tangent vector of the liquid-air interface, θ is the interface angle, whereas θ_c is the contact angle. Note that the value of γ and θ is dependent on the position along the contour of the surfer. (**b**) Upon actuation, the surface tension in the vicinity of the outlet becomes lower than that at other positions due to the mixing of the released surfactant. The contour in contact with the released surfactant (C_s) and the contour in contact with water (C_w) are illustrated with black and brown dotted lines, respectively. The reduced surface tension due to the surfactant release is denoted as γ_s, and the surface tension of the water is denoted as γ_w. (**c**) The structure of the embedded microfluidic channel in the Marangoni surfer includes a reservoir, nozzle/diffuser flow rectifiers at both inlet and outlet sides, an oscillatory ferrite rod (rod 1) attached to the moving elastic membrane, a stationary ferrite rod (rod 2) adhered to the substrate of the surfer, and a pump chamber. (**d**) Schematic of the working principle of the soft magnetic pump. (**d1**) The pumping mechanism is driven by the interaction force between two magnetically soft ferrite rods. When an external magnetic field ($\mathbf{B}_{ext}$) is applied, the ferrite rods are magnetized and exhibit magnetic moment ($\mathbf{m}_1$, $\mathbf{m}_2$), respectively. (**d2**) (inset) The magnetized ferrite rod 2 generates an induced magnetic field ($\mathbf{B}_2$) and thereby exerts a force ($\mathbf{F}_{12}$) on ferrite rod 1. (**d3**) The magnetic interaction force consequently deforms the elastic membrane and results in a displaced fluid volume (ΔV) flowing in the connecting nozzle/diffuser rectifiers. The flow rectifying effect of the nozzle/diffuser structures implies that the flow rate in the nozzle direction (Q_n) is smaller than that in the diffuser direction (Q_d) ensuring a net flow toward the outlet in each pumping cycle.

where $\mathbf{m}_1$ is the magnetic moment of rod 1 and $\mathbf{B}_2$ is the magnetic field of rod 2 induced by $\mathbf{B}_{ext}$ (Fig. 1d2). Consequently, the magnetic interaction force deforms a thin elastic membrane on top of the pump chamber and displaces the fluid volume, ΔV, in the connecting channels, resulting in a flow with lower flow rate in the nozzle direction (Q_n) and a flow with a higher flow rate in the diffuser direction (Q_d) (Fig. 1d3).

Combining the components described above, we are able to implement an untethered soft magnet-actuated microfluidic pump with a controllable flow rate. Furthermore, we can use it to demonstrate the controlled surfing

of the solutal Marangoni surfer. In the next section, the magnetic interaction force with regard to the applied magnetic field and the dimensions of the rods are discussed.

Magnetic interaction force

The first step toward the development of a soft magnetic pump is choosing an appropriate material. Here, we measure the magnetic hysteresis curve of two soft magnetic materials, manganese zinc ferrite (MnZn ferrite) and reduced iron, for comparison (Fig. 2a). A vibrating-sample magnetometer (GMW 3474-140, GMW, Redwood City, USA) is used to measure the magnetic hysteresis curve of the selected magnetic materials. The magnetic moment of the prepared samples (see insets in Fig. 2a) is measured by applying a magnetic field from -2 to 2×10^4 Oe and back to complete the hysteresis loop. The loop is carried out twice for each sample. The magnetic moment is the volumetric integral of the magnetization vectors of the soft magnetic rod,

$$\mathbf{m} = \int_V \mathbf{M}\, \mathrm{d}V, \tag{4}$$

where V denotes the volume of the soft magnetic rod. The magnetization of both materials as a function of the applied field can be seen in Fig. 2a. The achievable magnetization of the MnZn ferrite at 400 Oe, which is the maximum magnetic field that is applied in our magnetic actuation system[25], is approximately twice as high as that of the reduced iron-PDMS composite. Therefore, the MnZn ferrite is chosen to fabricate the soft magnetic rods. On the other hand, one can see from the hysteresis curve that the magnetic remanence for both soft magnetic

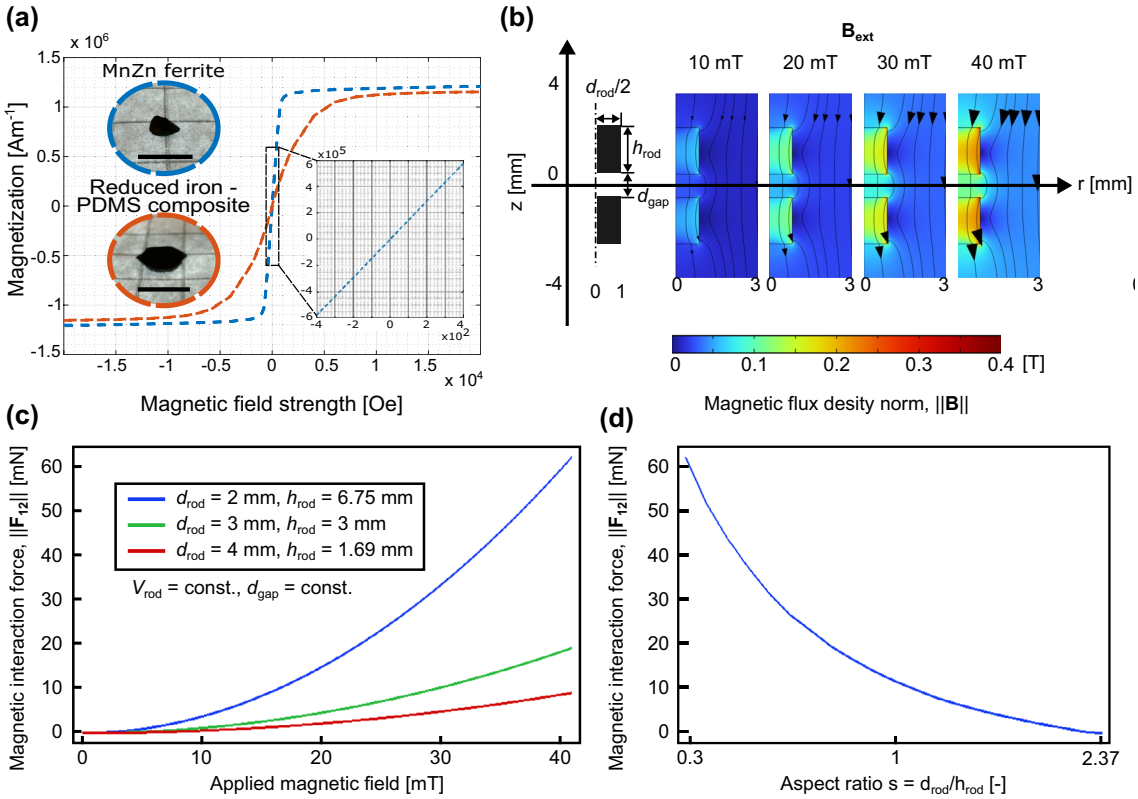

Fig. 2. Magnetic characterization of the soft magnetic rods and its resulting membrane deformation. (**a**) Vibrating-sample magnetometer measures the magnetic hysteresis loop of the selected soft magnetic materials: MnZn ferrite and reduced iron-polydimethylsiloxane composite. Scale bars in the insets are both 5 mm. Inset is a local zoom of the hysteresis curve of the MnZn ferrite around the origin, showing the low remanence of the selected soft magnetic material. (**b**) Finite element analysis results of the norm of the magnetic flux density field of MnZn ferrite rods subject to homogeneous external magnetic fields of different magnitudes. The corresponding magnetic field lines are plotted along with the arrowheads, whose size is proportional to the normalized field strength, and the orientation follows the direction of the local magnetic field. The diameter of the rod (d_{rod}), the height of the rod (h_{rod}), and the surface-to-surface distance, i.e., the gap (d_{gap}) between the rods are marked on the schematic drawing. (**c**) The influence of the aspect ratio ($s = d_{\mathrm{rod}}/h_{\mathrm{rod}}$) of the rod to the magnetic force is investigated. Under the condition that the volume of the rod (V_{rod}) and the gap distance (d_{gap}) are constants, we show the simulated results of the norm of magnetic interaction force ($\|\mathbf{F}_{12}\|$) when $d_{\mathrm{rod}} = \{2, 3, 4\}$ mm. The magnetic force is computed from the finite element model by integrating the Maxwell stress tensor over the surface of the rod. (**d**) Magnetic interaction force as a function of the aspect ratio of the soft ferrite rods.

materials is neglectable. Thus, the magnetic interaction force is zero, once the external magnetic field is removed, which allows us to switch off the pump.

Furthermore, an axisymmetric field model of the soft ferrite pairs under a homogeneous external magnetic field is presented. Fig. 2b shows the definitions of the model geometric parameters, where d_{rod} is the diameter of the rod ($d_{\text{rod}} = 2$ mm); h_{rod} is the height of the rod ($h_{\text{rod}} = 2$ mm); and d_{gap} is the surface-to-surface distance, i.e., the gap between the two rods ($d_{\text{gap}} = 1$ mm). The magnetic flux density at the presence of the external magnetic field ($\|\mathbf{B}_{\text{ext}}\| = \{10, 20, 30, 40\}$ mT) is computed with finite element methods (COMSOL Multiphysics 6.0, COMSOL Inc., Sweden) (Fig. 2b). The gradient of the induced magnetic field around the soft ferrite rods creates a local magnetic pulling force between them. Our next investigation involves the geometry of the soft ferrite rods. We define a dimensionless parameter, aspect ratio (s), as the ratio between the diameter and the height of the rod ($s = d_{\text{rod}}/h_{\text{rod}}$). We set the gap distance to 1 mm and keep the volume of the rod constant. Then, we compute the magnetic interaction force from the finite element model for the cases $d_{\text{rod}} = \{2, 3, 4\}$ mm (Fig. 2c). Next, the magnetic force as a function of the aspect ratio is plotted in Fig. 2d, where we can observe that a pair of slender rods with long axes aligned with the external magnetic field generates a higher magnetic interaction force than a pair of flat discs, for the same volume. In addition to the magnetic force, the membrane deformation should also be maximized while deciding which diameter and height the rod should have. In the next subsection, we numerically characterize the maximal displacement of the PDMS membrane under the exertion of the magnetic interaction force.

Membrane deformation

Based on the magnetic force model described in the previous section, the maximal deformation of the PDMS membrane can be derived as a consequence of the applied force. The thickness of the PDMS membrane is 150 μm and its diameter is 5 mm. Here, we investigate the magnetic force and maximal membrane deformation as a function of the diameter of the soft ferrite rod. The following parameters are controlled: the height of the rods is set to 2 mm, the applied external magnetic field is set to 40 mT, and the surface-to-surface distance between the rods is set to 1 mm. Since a long soft ferrite rod increases the chance of tilting the surfer due to their magnetic anisotropy, we limit the height of the rod to 2 mm. Figure 3a shows the representative cases of the simulation of the membrane deformation. In the simulated results, we can see that the magnetic interaction force is positively correlated to the diameter of the rod (Fig. 3b, blue line). On the other hand, the maximum membrane deformation shows a different trend as the diameter of the soft ferrite rod increases. One can see that the membrane deformation reaches its maximum when the rod diameter approaches 1.6 mm (Fig. 3b, red line). As the diameter is larger than 1.6 mm, despite the increase of the magnetic interaction force, the membrane deformation decreases. The explanation behind this result is the reduced deformable area on the membrane as the diameter of the ferrite rod increases. The deformable area on the membrane is determined by the area of the membrane, excluding the contact area with the soft ferrite rod. Due to the availability of the sintered soft ferrite rod, we incorporate the ferrite rods with a 2 mm diameter and a 2 mm height in our final design. After the optimal dimensions of the MnZn ferrite rods are determined, we further characterize the dynamic behavior of the membrane movement. In Fig. 3c, we compare the simulated results and the experimental validation of the membrane deformation. The membrane is driven by a square wave signal with 40 mT amplitude and 1 Hz frequency for 5 s. As shown in the plot, the maximal membrane deformation deducted from the model is 450 μm, whereas the measurements only show around 200 μm. Such mismatch can be the result of the insufficient pre-tension of the membrane, i.e., the membrane is loose after the manual assembly of the device.

Flow rectifying nozzle/diffuser structure

The operation of the magnetic pump is driven by the oscillatory pumping action induced by the periodic driving signal, i.e., a switching external magnetic field. A full pumping cycle consists of two phases: a pumping phase and a suction phase. The pumping phase is where a non-zero external magnetic field is applied and an attractive interaction force occurs between the MnZn ferrite rods, causing the deformation of the membrane. On the other hand, the suction phase is where the external magnetic field is removed and the membrane recovers its initial shape due to its elastic restoring force. During the pumping phase, surfactant stored in the pump chamber is discharged in both directions (toward the inlet and the outlet). If the flow rates in both directions do not differ, no net flow is generated from the inlet to the outlet. Hence, a flow-rectifying solution needs to be implemented to ensure the proper function of the magnetic pump.

A typical implementation of flow rectifiers involves microfluidic check valves with movable components[26]. This category of flow rectification mechanism significantly reduces the backflow but requires sufficient pressure to open the movable check valve. An alternative is a valveless rectification pump, which does not include movable components such as check valves. Instead, the flow rectification is achieved through the specific channel geometry that allows asymmetric flow resistances in opposite flow directions[27]. Amongst all the valveless flow rectifiers, nozzle/diffuser channels have a simple geometry and have been widely used in numerous previous studies[28–30]. A nozzle/diffuser structure is a taper-shaped channel with a smaller channel width at the nozzle side (w_{n}) and a larger channel width at the diffuser side (w_{d}). Due to the wall–fluid interaction, the flow rate in the nozzle direction (Q_{n}) is lower than that in the diffuser direction (Q_{d}) (Fig. 4a). Considering the flow in the diffuser direction, the relationship between the pressure drop across the nozzle/diffuser structure and the magnitude of the flow velocity can be expressed as[29],

$$\mathbf{v}_{\text{d}} = \sqrt{\frac{2\Delta p}{\rho K_{\text{d}}}}, \tag{5}$$

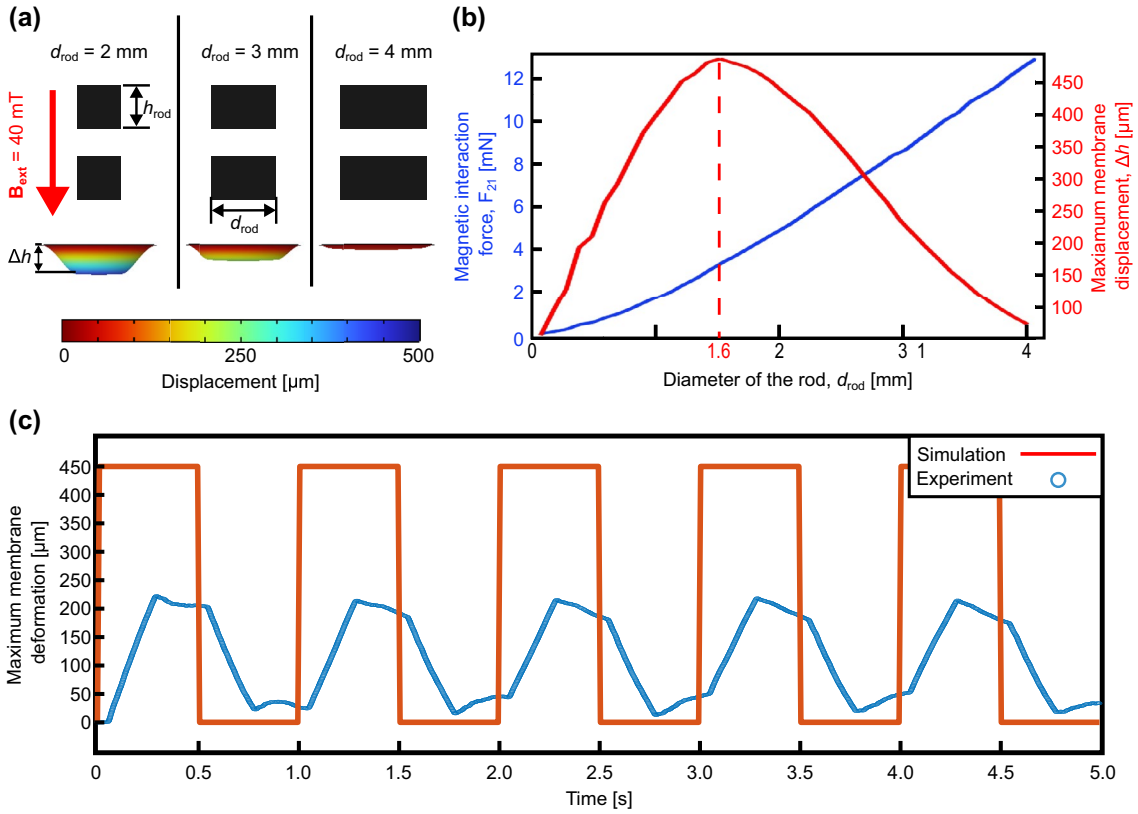

Figure 3. Modeling of the maximal membrane deformation with regard to the rod diameter. (**a**) Model of the displacement of a 150 μm thick PDMS membrane with a diameter of 5 mm deformed by MnZn ferrite rods with various diameters ($d_{rod} = \{2, 3, 4\}$ mm) and a constant height ($h_{rod} = 2$ mm). In the simulation, boundary stresses are determined by the computed magnetic force with given rod dimensions under the 40 mT external field. For simplicity, the elasticity of the membrane is assumed linear. (**b**) Magnetic interaction force and membrane deformation as functions of the diameter of the MnZn ferrite rod. As shown, the maximal membrane deformation occurs when the diameter of the soft ferrite rod is 1.6 mm. (**c**) Comparison of the simulated and the experimental results of the membrane deformation driven by a square wave signal with the amplitude of 40 mT and a frequency of 1 Hz for 5 s. The maximum membrane deformation derived from the simulation reaches 450 μm, whereas the experimental results measures around 200 μm.

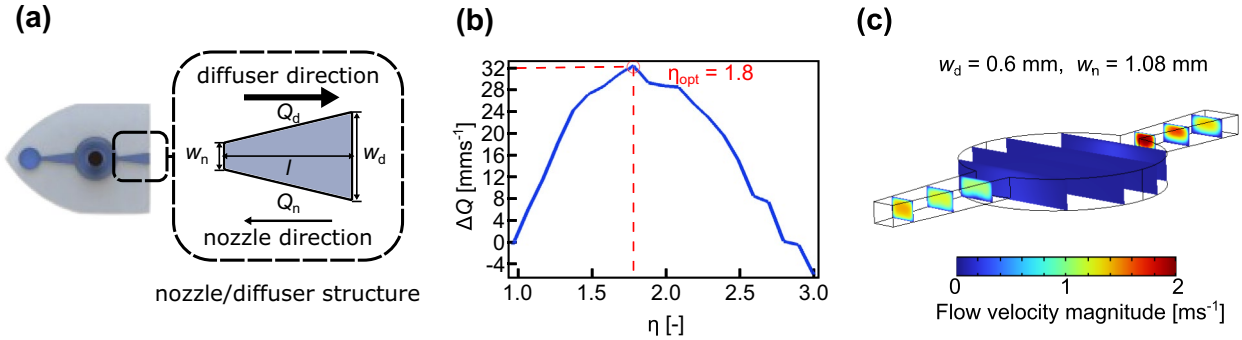

Figure 4. Flow rectifying nozzle/diffuser structure for valveless pump. (**a**) Geometrical parameters of the nozzle/diffuser structure, w_n and w_d denotes the nozzle and diffuser width, respectively, and l is the length of the nozzle/diffuser. (**b**) The simulated results of the flow rectification efficacy with regard to the channel geometry. We choose the case where the rods are 2 mm in diameter and 2 mm in height with a 1 mm surface-to-surface distance for this model, yielding a boundary stress (4.64 mN distributed across a circle with 2 mm diameter) applied to the top surface of the pump chamber. A dimensionless number (η) is defined as the ratio between the diffuser and nozzle width to describe the opening angle of the channel. Under the condition of a constant nozzle width ($w_n = 0.6$ mm), the net flow rate (ΔQ) as a function of η is computed. One can locate the local optimum at $\eta_{opt} = 1.8$, which corresponds to a diffuser width of 1.08 mm. (**c**) Flow velocity magnitude profiles of selected cross-sections in the channel with the chosen dimensions ($(w_d, w_n) = (1.08, 0.6)$ mm). The maximum flow velocity based on the simulated result reaches 1.97 m s^{-1}.

where Δp is the pressure drop across the nozzle/diffuser structure, v_d is the magnitude of the flow velocity at the diffuser side cross-section, K_d is the pressure loss coefficient in the diffuser direction, ρ is the density of the working fluid. Similarly, the magnitude of the flow velocity at the nozzle side cross-section can be determined with,

$$\mathbf{v}_n = \sqrt{\frac{2\Delta p}{\rho K_n}}, \tag{6}$$

where v_n is the magnitude of the flow velocity at the nozzle side cross-section, and K_n is the pressure loss coefficient in the nozzle direction. Furthermore, we compute the volumetric flow rate of the cross-section of interest by integrating the flow velocity across the cross-sectional area,

$$Q_d = \iint_A \mathbf{v}_d \cdot \, d\mathbf{A}_d, \tag{7}$$

where Q_d is the volumetric flow rate at the diffuser side cross-section, $\mathbf{A}_d$ is the cross-sectional area vector with its direction normal to the cross-section at the diffuser side. Likewise, we obtain the volumetric flow rate at the nozzle side (Q_n) via

$$Q_n = \iint_A \mathbf{v}_n \cdot \, d\mathbf{A}_n, \tag{8}$$

where $\mathbf{A}_n$ is the cross-sectional area vector with its direction normal to the cross-section at the nozzle side cross-section. The performance of a flow rectifier can be assessed by the net flow generated in the desired direction, which, in our case, is the diffuser direction. On this account, the net flow rate (ΔQ) is defined as,

$$\Delta Q = Q_d - Q_n. \tag{9}$$

One factor that affects the diodity of the nozzle/diffuser flow rectifier is its geometry. We numerically investigate the relationship between the geometrical parameters of a nozzle/diffuser and the net flow rate with the help of a computational fluid dynamics model (COMSOL Multiphysics 6.0, COMSOL Inc., Sweden). In this regard, we define the ratio of the diffuser width (w_d) and the nozzle width (w_n) as a dimensionless number (η) to describe the opening angle of the nozzle/diffuser. In the simulation model, the nozzle width, and channel length are set as constant values of 0.6 mm and 3.6 mm, respectively. The channel height is 0.5 mm. It is assumed that the pump is actuated by the rods with 2 mm height and 2 mm diameter under 40 mT external magnetic field, which exerts 4.64 mN to the attached membrane. In Fig. 4b, one can see that the maximal net flow rate of 32 $mm^3 s^{-1}$ occurs when η_{opt} is 1.8, which corresponds to a diffuser width of 1.08 mm. Noteworthily, the net flow rate does not monotonically increase as the dimensionless number (η) increases. In contrast, when η is larger than 1.8, the net flow rate drops. Furthermore, the net flow rate becomes negative when η exceeds 2.8, which indicates a larger return flow than a forward flow. Finally, the chosen channel widths are $(w_n, w_d) = (0.6, 1.08)$mm. Figure 4c shows a flow velocity magnitude at various cross-sections in the channel of the chosen design.

Another limiting factor of a valveless flow rectifier is its performance at low Reynolds number ($Re = \frac{\rho UL}{\mu}$) regime, which is determined by the density of the fluid (ρ), the velocity of the flow (U), the characteristic length (L), and the dynamic viscosity of the fluid (μ). In the case of Newtonian fluids, when Reynold's number gets significantly smaller, especially when it enters the Stokes flow regime ($Re \ll 1$), the non-linear terms in the Navier Stokes equation disappears, rendering the flow resistance in the channel isotropic. This being said, when the Stokes flow regime applies, the flow is reversible, so no rectification effect can be achieved. Different approaches have been investigated to re-introduce the non-linearity such that flow rectification occurs. These include relying on the viscoelasticity of the liquid and using deformable channel walls[31–33]. For a better understanding of the flow regime our system belongs to, an estimation of the Reynolds number of our device is made. The density of the isopropyl alcohol (IPA) solution is calculated based on the concentration (957 kg m^3), and the dynamic viscosity is approximated to be 0.002 cPs based on the curve provided by a previous work[34]. Based on Fig. 4c, we obtain a maximum flow velocity of 1.97 m s^{-1}, and a minimum flow velocity of close to 0 m s^{-1}. We choose the average flow velocity of 1 m s^{-1} and determine the characteristic length as 0.5 mm based on the channel height. Finally, the computed Reynolds number is 239.3, which is higher than in the creep flow regime but still in the laminar flow regime.

Experimental validation: untethered soft magnetic pump

Based on the design considerations and the chosen parameters discussed in the previous subsections, we employ a pair of MnZn ferrite rods with a diameter of 2 mm and a height of 2 mm, a PDMS membrane with a thickness of 150 µm and nozzle/diffuser flow rectifiers with the nozzle channel width (w_n) of 0.6 mm and diffuser channel width (w_d) of 1.08 mm. A test platform for the soft magnetic pump is built according to these chosen parameters. We connect the soft magnetic pump with a reservoir containing dyed isopropyl alcohol (IPA) solution (volume ratio water: IPA = 5:1) at the inlet side and connected to a serpentine channel for measuring the flow rate (Fig. 5a). The dyed IPA solution is prefilled to the starting point of the serpentine channel suctioning with a syringe connected to the outlet. Square wave signals with an amplitude of 40 mT and frequencies ranging from 1 to 25 Hz are applied. Note that the frequency sweep consists of 1 Hz-steps from 1 to 10 Hz and 5 Hz-steps from 10 to 25 Hz. As a representative case, Fig. 5b shows the movement of the fluid when the pump is driven at 8 Hz. The advancing of the fluid front can be clearly seen in the figure. We can then calculate the time needed to fill the serpentine channel, thereby deducing the average volumetric flow rate. The results of the average flow rate with regard to the driving frequencies are illustrated in Fig. 5c. At the driving frequency of 8 Hz, the pump

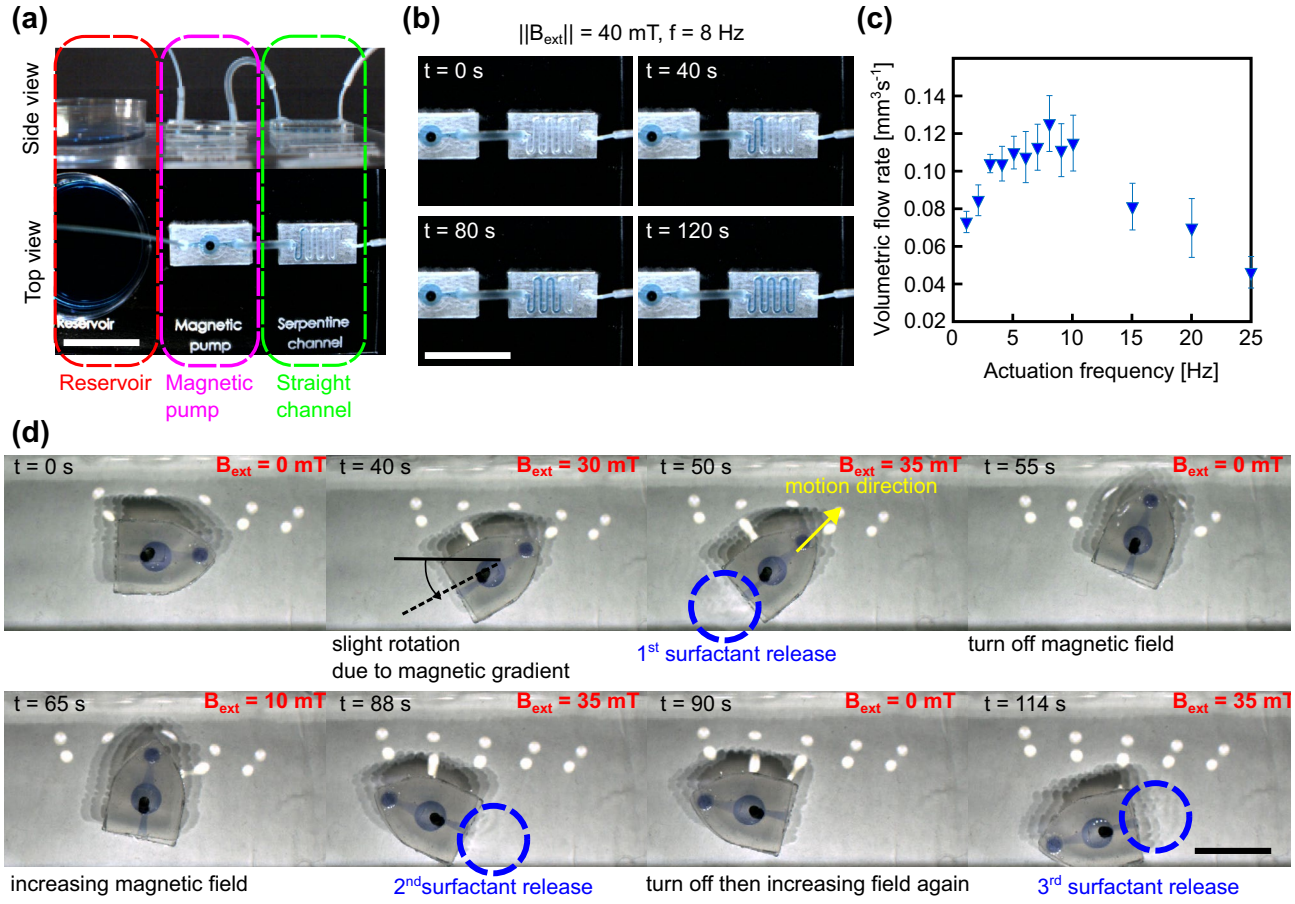

Figure 5. Demonstration of an untethered magnetic pump and microfluidics-based Marangoni surfer. (**a**) Top and side views of the experimental setup. The setup includes a reservoir, a magnetic pump, and a serpentine channel to measure the flow rate. Scale bar is 20 mm. (**b**) Time stamps of the soft magnetic pump in action. The waveform of the actuating signal is a square wave with an amplitude of 40 mT at various frequencies. In this representative case, the pump is driven at 8 Hz. Scale bar is 20 mm. (**c**) Characterization of the pump flow rate with regard to the actuation frequency. At the actuation frequency of 8 Hz, the pump exhibits the highest volumetric flow rate, which is 0.13 mm^3s^{-1}. As the actuation frequency further increases, the volumetric flow rate drops significantly.(**d**) Time stamps of the motion experiments of microfluidics-based Marangoni surfer. The surfer remains static when no external magnetic field is applied. Next, the magnetic field strength is gradually increased with manual control, where a slight rotation of the surfer due to the inhomogeneity of the magnetic field can be observed. The surfactant stored in the pump chamber is released and propels the surfer in the motion direction when the magnetic field reaches 35 mT. The surfactant release can be observed by the ripples induced by the solutal Marangoni convection (Supplementary Movie). These experimental processes are repeated three times to showcase the multi-step surfactant release, demonstrating the possibility of using the proposed untethered pump for the controlled release of the surfactant. Scale bar is 20 mm.

exhibits the highest volumetric flow rate of 0.13 mm^3s^{-1}, whereas at the higher driving frequencies, the flow rate significantly drops (0.07 mm^3s^{-1} at 20 Hz and 0.05 mm^3s^{-1} at 25 Hz). The explanation for this observation can be that the oscillation of the system can not keep up with actuation at higher driving frequencies. Footages of the pump experiments can be found in the Supplementary Movie. To take advantage of the untetheredness of the proposed device, we integrate the pump into a Maranogi surfer to further demonstrate its controllability over the surfactant release with a stop-and-move motion.

Experimental validation: motion experiment of the untethered Marangoni surfer

Leveraging on the untetheredness of the proposed soft magnetic pump, we further explore the possibility of integrating the pump into a microfluidics-based Marangoni surfer. However, the oscillatory pumping action introduces disturbance to a floating device. For this reason, the magnitude of the external magnetic field driving the Marangoni surfer is manually controlled and increased/decreased in steps of 1 mT to avoid jerking motion. The maximal volume that can be discharged from the pump chamber depends on the maximal deformation of the membrane. To achieve this, we replace the channel layer and the membrane layer with one monolithic piece of silicone rubber (Ecoflex™00-20, Smooth-On, USA) that is more elastic than PDMS. Yet, since the membrane is monolithically molded as part of the channel structure, the minimal thickness that can be achieved with this

fabrication method is 0.3 mm. Based on the COMSOL model built for the PDMS membrane, we adopt the membrane thickness and the material properties (Young's modulus 125 kPa and Poisson ratio 0.3) for the Ecoflex 00-20. This allows us to compute the maximal membrane deformation, which is 860 μm under the same actuation conditions (464 mN magnetic interaction force achieved by the soft ferrite rods with 2 mm height and 2 mm diameter, and the magnitude of the applied magnetic field 40 mT). Time stamps of the motion experiment are shown in Fig. 5d. The experiment starts in the static state without the application of the magnetic field, where no motion of the surfer can be observed. Next, we gradually increase the magnitude of the magnetic field strength, and a slight rotation of the surfer occurs. The possible reason is the magnetic pulling force generated by the inhomogeneity of the magnetic field and the torque caused by the misalignment of the magnetization with the field. When the magnetic field reaches the value of 35 mT, the accumulated pressure of the liquid overcomes the pressure barrier created by the sudden widening of the outlet, and the surfactant can be released to the air-water interface. The release of the surfactant induces the Marangoni convection at the interface and propels the surfer in the motion direction. One can observe the surfactant release through the ripples on the water surface in Fig. 5d. Finally, we switch off the magnetic field gradually to stop the surfactant release without introducing disturbance to the surfer. Consequently, the surfer resumes to its static state and no motion can be observed thereon. After the first surfactant release, we repeat these processes three times to showcase the stop-and-move motion of the surfer (see Fig. 5d). In contrast to the majority of the previous solutal Marangoni surfers, whose surfactant release can not be controlled, we demonstrate the multi-step surfactant release enabled by the controlled surfactant release. The recording of the motion experiment is enclosed in the Supplementary Movie.

Conclusions and future work

In this work, we present a novel pumping mechanism that allows the contactless actuation of a magnetic micropump. We demonstrate the application of the pump as a desktop microfluidic device, as well as an integrated part of an untethered microfluidics-based Marangoni surfer. We also numerically investigate the magnetic interaction forces between a pair of soft ferrite rods in the presence of an external magnetic field, the membrane deformation corresponding to the force exerted by the soft ferrite rods, and the performance of the nozzle/diffuser flow rectifier with regard to its geometrical parameters to support our design choices.

Moving toward future practical application of the Marangoni surfer, the working space and lifetime of the surfer are crucial factors. Currently, the working space is limited by the diameter of the external Helmholtz coils. This limitation can be overcome by introducing an onboard electromagnetic component, such as a planar electromagnetic coil[35]. This component allows the switching of magnetic field direction without relying on external coils. However, this approach requires an energy source and a control unit. They can either be offboard, restricting the working space to the wire length, or be onboard, adding extra weight and hindering the miniaturization of the device. Hence, the authors envision further miniaturization of the Marangoni surfer for use in micro-manipulation within the confines of a desktop Helmholtz coils setup. On the other hand, the lifetime of the Marangoni surfer is determined by the size of the reservoir and the surfactant release rate. Extending the lifetime with a larger reservoir increases the weight and size of the surfer, which may be undesirable for some applications. Alternatively, reducing the surfactant release rate by adjusting the actuation frequency could prolong the lifetime but may compromise surfing speed. Another design variation is the surfactant. In this study, IPA is chosen based on its wide availability. Other surfactants with lower surface tension than water can also generate non-zero direct Marangoni force based on Eq. 2. Surfactants with other properties, such as biocompatibility or low volatility, can be further investigated for specific applications.

Regarding the scalability of the soft magnetic pump, the magnetic force applied scales directly with the square of the volume and inversely with the fourth power of the center-to-center distance. Although miniaturizing such devices will drastically reduce the magnetic interaction force, a locally applied high magnetic field could compensate for the loss of the force. The natural frequency of the membrane is another factor to be investigated in further studies. Having a better understanding of the contributing factors to the frequency response of the membrane can help us develop a frequency-selective actuation strategy by fabricating membranes with different natural frequencies. A systematic characterization of the frequency response can enable a model-based design of the soft magnetics-driven microfluidic pump. In the future study, we aim to explore the parallel actuation and selective actuation modalities of the proposed magnetic pump and demonstrate its applications, such as culturing cells with constant circulating flow or with enhanced media exchange enabled by the pumping action.

Methods

Simulation of the membrane deformation model

The membrane deformation in this study is calculated using the *Plate Interface* of the *Structural Mechanics Module* in the finite element analysis software (COMSOL Multiphysics 6.0, COMSOL Inc., Sweden). The material properties of PDMS are adopted from the COMSOL materials library, with a Young's modulus of 750 kPa and a Poisson's ratio of 0.49, assuming the material is linear and isotropic. The membrane is circular, with a diameter of 5 mm and a thickness of 150 μm. The contact area, where the membrane interfaces with the MnZn ferrite rod, is marked as a concentric circle of varying diameters with the membrane. Since this area adheres to the surface of the solid surface of MnZn ferrite, it is assumed to have no rotation, meaning the displacement of the shell normal is set to zero. Furthermore, the boundary of the membrane possesses fixed constraints, implying that the displacement, the displacement of the shell normal, and their first-time derivatives are all zero. Finally, a face load derived from the computed magnetic interaction force over the contact area is applied

Simulation of the flow rectifying nozzle/diffuser structure

The influence of the geometry of the nozzle/diffuser flow rectifier on the rectification efficiency in this study is numerically investigated using the Laminar Flow interface of the Fluid Flow module in COMSOL. This interface deals with the flow whose Reynold's number falls into the laminar flow regime, i.e., ranging from around 1 to 2000. The liquid property is chosen as water for simplicity from the material library. The geometry of the channel is imported using LiveLink for Solidworks. The governing equations are the Navier–Stokes equations based on the conservation of momentum and the equation for the conservation of mass. Lastly, boundary stress derived by dividing the computed magnetic interaction force with the contact area is applied at the channel where the membrane is located.

Fabrication of the soft magnetic pump

The proposed microfluidics-based Marangoni surfer is constructed in a layer-by-layer fashion, similar to a conventional microfluidic device. The channel layer is created using a 500 µm thick polycarbonate plate (LEXAN™ 8010MC, Sabic Innovative Plastics™, The Netherlands), while a 2 mm thick polymethyl methacrylate (PMMA) plate serves as the substrate layer. To ensure a secure seal between the substrate and the channel, a double-sided medical-grade pressure-sensitive adhesive (ARcare® 90106NB, Adhesives Research Inc., Ireland) is used to bond the layers. The structure and design of each layer are patterned with a CO_2 laser cutter.

The next step involves fabricating a thin elastic membrane with polydimethylsiloxane (PDMS) (Sylgard 184, Farnell, United Kingdom), a commonly used elastomer in microfluidics. Initially, we laser cut a 150 µm thick polyethylene terephthalate (PET) foil into a substrate and a mold with the required dimensions for the membrane. These two parts are then securely taped to prevent any leakage. Subsequently, the PDMS monomer (part A) and the cross-linker (part B) are mixed at a volume ratio of 10:1 and degassed in a desiccator for 5 min. The degassed PDMS is poured onto the mold, spread evenly, and baked in an oven at 70° for 60 min. Finally, the 150 µm PDMS membranes can be demolded and bonded to the channel layer with a patterned adhesive layer. Besides the basic components, a pair of the MnZn ferrite rods (Material 77, Part No. 3078990851, Fair-Rite Products Corp., USA) are affixed to the top and bottom of the pump chamber with the help of the double-sided adhesive.

Fabrication process of the Marangoni surfer

The channel layer and the substrate layer of the miniature Marangoni surfer are fabricated separately and then assembled with medical-grade microfluidic adhesive layers. Firstly, the channel layer is molded with elastic silicone rubber to ensure sufficient membrane deformation (Ecoflex™ 00-20, Smooth-On, USA). The mold for the channel layer is printed by a stereolithography 3D printer using clear resin (Clear Resin V4, Formlabs, USA). After printing, the mold is sonicated in isopropyl alcohol for 10 minutes and then exposed to UV light for curing. To ensure the residual resin is completely removed, the mold is post-baked at 120 °C for 2 h. Next, the mold release agent is sprayed on the mold and left to dry for around 30 minutes. Ecoflex™ 00-20 is mixed (weight ratio A: B = 1: 1) and degassed in a desiccator for 5 min. To mold the channel layer, the Ecoflex™ 00-20 is poured into the mold, which has the negative contour of the channel layer design, and is baked in the oven at 70 °C for 2 h. A pattered channel layer can be demolded after curing in the oven.

Secondly, a substrate with a hole at the corresponding position of the ferrite rod is prepared. The substrate is a 2 mm thick PMMA plate laser cut by CO_2 laser. Thirdly, two MnZn soft ferrite rods are cut into the desired length. Here, 2 mm long ferrite rods are used in the design. Next, the last layer to be prepared is the bonding layer, which is also laser cut into the desired pattern. Finally, the robot is assembled layerwise. The channel layer is first bonded to the substrate and followed by mounting the soft ferrite rods at the center of the pump chamber also with the help of the double-sided tape.

Experimental setup

For the characterization of the magnetic pump and the motion experiments of the Marangoni surfer, a Helmholtz coil setup is used[25]. The movies of the experiments are recorded with complementary metal-oxide-semiconductor (CMOS) cameras with a frame rate of 30 frames-per-second (FLIR Blackfly S USB3 camera, Teledyne FLIR LLC, USA).

The dynamic behavior of the membrane deformation is measured by a laser displacement sensor (optoNCDT ILD1402, Micro-Epsilon Messtechnik GmbH & Co. KG, Germany) mounted vertically above the membrane. A user interface (sensorTOOL v1.12.0.1370, Micro-Epsilon Messtechnik GmbH & Co. KG, Germany) is used to capture the sensor readout, the temporal resolution of the laser displacement sensor is 7 µs.

Data availability

The data that support the plots within this paper and other findings of this study are available from the author upon reasonable request.

Received: 7 February 2024; Accepted: 22 August 2024
Published online: 31 August 2024

References

1. Zhong, Q., Ding, H., Gao, B., He, Z. & Gu, Z. Advances of microfluidics in biomedical engineering. *Adv. Mater. Technol.* **4**, 1800663. https://doi.org/10.1002/ADMT.201800663 (2019).
2. Yang, Y. *et al.* Microfluidics for biomedical analysis. *Small Methods* **4**, 1900451. https://doi.org/10.1002/SMTD.201900451 (2020).
3. Preetam, S. *et al.* Emergence of microfluidics for next generation biomedical devices. *Biosens. Bioelectron.: X* **10**, 100106. https://doi.org/10.1016/J.BIOSX.2022.100106 (2022).

4. Ortseifen, V., Viefhues, M., Wobbe, L. & Grünberger, A. Microfluidics for biotechnology: Bridging gaps to foster microfluidic applications. *Front. Bioeng. Biotechnol.* **8**, 589074. https://doi.org/10.3389/FBIOE.2020.589074/BIBTEX (2020).
5. Laser, D. J. & Santiago, J. G. A review of micropumps. *J. Micromech. Microeng.* **14**, R35. https://doi.org/10.1088/0960-1317/14/6/R01 (2004).
6. Oh, K. W. & Ahn, C. H. A review of microvalves. *J. Micromech. Microeng.* **16**, R13. https://doi.org/10.1088/0960-1317/16/5/R01 (2006).
7. Li, W. *et al.* A review of recent studies on valve-less piezoelectric pumps. *Rev. Sci. Instrum.* **94**, 031502. https://doi.org/10.1063/5.0135700 (2023).
8. Tang, S.-Y. *et al.* Liquid metal enabled pump. *Proc. Natl. Acad. Sci.* **111**, 3304–3309. https://doi.org/10.1073/pnas.1319878111 (2014).
9. Araci, I. E. & Quake, S. R. Microfluidic very large scale integration (mVLSI) with integrated micromechanical valves. *Lab Chip* **12**, 2803–2806. https://doi.org/10.1039/C2LC40258K (2012).
10. Azizbeigi, K., Zamani Pedram, M. & Sanati-Nezhad, A. Microfluidic-based processors and circuits design. *Sci. Rep.* **11**, 10985. https://doi.org/10.1038/s41598-021-90485-z (2021).
11. Filippi, M., Yasa, O., Kamm, R. D., Raman, R. & Katzschmann, R. K. Will microfluidics enable functionally integrated biohybrid robots?. *Proc. Natl. Acad. Sci. U.S.A.* **119**, e2200741119. https://doi.org/10.1073/pnas.2200741119 (2022).
12. Gao, R. Z. & Ren, C. L. Synergizing microfluidics with soft robotics: A perspective on miniaturization and future directions. *Biomicrofluidics.* **12**, 011302. https://doi.org/10.1063/5.0036991 *(2021).*
13. Ilievski, F., Mazzeo, A. D., Shepherd, R. F., Chen, X. & Whitesides, G. M. Soft robotics for chemists. *Angew. Chem.* **123**, 1930–1935. https://doi.org/10.1002/ange.201006464 (2011).
14. Shepherd, R. F. *et al.* Multigait soft robot. *Proc. Natl. Acad. Sci. U.S.A.* **108**, 20400–20403. https://doi.org/10.1073/pnas.1116564108 (2011).
15. Katzschmann, R. K., Delpreto, J., Maccurdy, R. & Rus, D. Exploration of underwater life with an acoustically controlled soft robotic fish. *Sci. Robot.* **3**, 3449. https://doi.org/10.1126/scirobotics.aar3449 (2018).
16. Kwak, B., Choi, S., Maeng, J. & Bae, J. Marangoni effect inspired robotic self-propulsion over a water surface using a flow-imbibition-powered microfluidic pump. *Sci. Rep.* **11**, 17469. https://doi.org/10.1038/s41598-021-96553-8 *(2021).*
17. Bush, J. W. M. & Hu, D. L. Walking on water: Biolocomotion at the interface. *Annu. Rev. Fluid Mech.* **38**, 339–369. https://doi.org/10.1146/annurev.fluid.38.050304.092157 (2005).
18. Lauga, E. & Davis, A. M. Viscous Marangoni propulsion. *J. Fluid Mech.* **705**, 120–133. https://doi.org/10.1017/jfm.2011.484 (2012).
19. Ender, H., Froin, A. K., Rehage, H. & Kierfeld, J. Surfactant-loaded capsules as Marangoni microswimmers at the air-water interface: Symmetry breaking and spontaneous propulsion by surfactant diffusion and advection. *Eur. Phys. J. E.* **44**, 1–22. https://doi.org/10.1140/epje/s10189-021-00035-8 (2021).
20. Dietrich, K., Jaensson, N., Buttinoni, I., Volpe, G. & Isa, L. Microscale Marangoni surfers. *Phys. Rev. Lett.* **125**, 098001. https://doi.org/10.1103/PhysRevLett.125.098001 *(2020).*
21. Yoshida, K. & Onoe, H. Marangoni-propulsion micro-robots integrated with a wireless photonic colloidal crystal hydrogel sensor for exploring the aquatic environment. *Adv. Intell. Syst.* **4**, 2100248. https://doi.org/10.1002/aisy.202100248 *(2022).*
22. Gray, B. L. A review of magnetic composite polymers applied to microfluidic devices. *J. Electrochem. Soc.* **161**, B3173–B3183. https://doi.org/10.1149/2.023402jes (2014).
23. Diller, E., Miyashita, S. & Sitti, M. Remotely addressable magnetic composite micropumps. *RSC Adv.* **2**, 3850–3856. https://doi.org/10.1039/C2RA01318E (2012).
24. Scriven, L. & Sternling, C. The Marangoni effects. *Nature* **187**, 186–188. https://doi.org/10.1038/187186a0 (1960).
25. Thomas, T. L., Sikorski, J., Ananthasuresh, G. K., Venkiteswaran, V. K. & Misra, S. Design, sensing, and control of a magnetic compliant continuum manipulator. *IEEE Trans. Med. Robot. Bionics* **4**, 910–921. https://doi.org/10.1109/TMRB.2022.3204577 (2022).
26. Qian, J.-Y., Hou, C.-W., Li, X.-J. & Jin, Z.-J. Actuation mechanism of microvalves: A review. *Micromachines* **11**, 172. https://doi.org/10.3390/mi11020172 (2020).
27. Tesař, V. & Li, D. Valve-less rectification pumps. In *Encyclopedia of Microfluidics and Nanofluidics* (ed. Li, D.) 2132–2139. https://doi.org/10.1007/978-0-387-48998-8_1656 (2008).
28. Nguyen, N.-T., Huang, X. & Chuan, T. K. Mems-micropumps: A review. *J. Fluids Eng.* **124**, 384–392. https://doi.org/10.1115/1.1459075 (2002).
29. Olsson, A., Stemme, G. & Stemme, E. Numerical and experimental studies of flat-walled diffuser elements for valve-less micropumps. *Sens. Actuators, A* **84**, 165–175. https://doi.org/10.1016/S0924-4247(99)00320-9 (2000).
30. Olsson, A., Stemme, G. & Stemme, E. Diffuser-element design investigation for valve-less pumps. *Sens. Actuators, A* **57**, 137–143. https://doi.org/10.1016/S0924-4247(97)80104-5 (1996).
31. Sousa, P., Pinho, F., Oliveira, M. & Alves, M. Efficient microfluidic rectifiers for viscoelastic fluid flow. *J. Nonnewton. Fluid Mech.* **165**, 652–671. https://doi.org/10.1016/j.jnnfm.2010.03.005 (2010).
32. Groisman, A. & Quake, S. R. A microfluidic rectifier: Anisotropic flow resistance at low Reynolds numbers. *Phys. Rev. Lett.* **92**, 094501. https://doi.org/10.1103/PhysRevLett.92.094501 (2004).
33. Mehboudi, A. & Yeom, J. A passive stokes flow rectifier for Newtonian fluids. *Sci. Rep.* **11**, 10182. https://doi.org/10.1038/s41598-021-89699-y (2021).
34. Park, J.-G. *et al.* Interfacial and electrokinetic characterization of IPA solutions related to semiconductor wafer drying and cleaning. *J. Electrochem. Soc.* **153**, G811. https://doi.org/10.1149/1.2214532 (2006).
35. Richter, M. *et al.* Locally addressable energy efficient actuation of magnetic soft actuator array systems. *Adv. Sci.* **10**, 2302077. https://doi.org/10.1002/advs.202302077 (2023).

Acknowledgements

This work is supported by the European Research Council (ERC) under the European Union's Horizon 2020 Research and Innovation programme under Grant 866494 project - MAESTRO.

Author contributions

Y.H.L. conceived and conducted the experiments. Y.H.L. designed and fabricated the soft magnetic pump and the Marangoni surfer. Y.H.L., F.N.P.B., and V.K.V. analyzed and interpreted the numerical and experimental results. V.K.V. and S.M. supervised the project. S.M. acquired the research funding and provided research facilities. Y.H.L. drafted the first manuscript. S.M. reviewed and commented on the manuscript and rebuttal. All authors read, corrected, and approved the final manuscript.

Competing interests

The authors declare no competing interests.

Additional information

Supplementary Information The online version contains supplementary material available at https://doi.org/10.1038/s41598-024-70944-z.

Correspondence and requests for materials should be addressed to Y.-H.L. or S.M.